Comparison of novel Ni doped exsolution perovskites as methane dry reforming catalysts

L. Lindenthal[1], *F*. Schrenk[1], *R*. Rameshan[1], *C*. Rameshan[1], *L*. Kronlachner[2], and *A*. Nenning[2]

[1]Technische Universität Wien, Institute of Materials Chemistry, Vienna, Austria
[2]Technische Universität Wien, Institute of Chemical Technologies and Analytics, Vienna, Austria

Abstract: Three perovskite-type materials with a different amount of B-site Ni doping have been tested for their catalytic performance during methane dry reforming (MDR) followed by characterization with X-ray diffraction (XRD) and scanning electron microscopy (SEM). They could be activated via a reductive treatment (either during a pre-reduction step or directly in reducing reaction atmosphere), the main activating mechanism being the formation of Ni nanoparticles on the surface by exsolution. The catalytic activity increased with the particle size and density. The particle distribution properties could be improved by increasing the amount of Ni doping from 3 % to 10 %, by using an A-site sub-stoichiometric perovskite and by choosing a higher annealing temperature during material preparation. A deactivation over time was observed, due to segregation of $CaCO_3$ on the surface, but no coking or particle sintering occurred

1 Introduction

The catalytic reaction of methane with carbon dioxide, which is commonly referred to as methane dry reforming (MDR, Equation 1), is an interesting process because it combines the use of two prominent greenhouse gases (CH_4 and CO_2) with the production of the technologically valuable synthesis gas, a mixture of H_2 and CO.

$$CH_{4(g)} + CO_{2(g)} \rightleftharpoons 2\,H_{2(g)} + 2\,CO_{(g)} \quad (1)$$

The reaction was first described in 1928 by Fischer and Tropsch over Ni and Co catalysts. A severe problem they encountered was the carbon deposition on the catalyst and the following deactivation. However, MDR has a significantly lower energy consumption compared to other methane reforming processes and a product ratio suitable for direct conversion of the formed synthesis gas into further valuable products such as long chain hydrocarbons (via the Fischer-Tropsch process) or methanol [1]. Dry reforming can also easily be extended from methane to other hydrocarbons, making the reaction very important for the processing of natural gas resources or renewable feedstocks such as biogas [2].

Studies of different metal catalysts for MDR have shown that noble metals such as Ru, Pd, Rh, Pt and Ir show a high catalytic activity [3,4]. A cheaper alternative to noble metals is the use of Nickel based catalysts, specifically systems that form catalytically active Nickel particles in reaction conditions such as Ni-doped Perovskites [5]. A proposed mechanism

for MDR includes the activation of CH_4 via degradation into C and H_2[1]. This degradation would normally only take place above 550 °C, but the presence of a catalyst allows it to happen at lower temperatures by forming intermediates like CH_x or formyl groups [6,7]. These intermediates then react with oxygen species on the surface to yield CO and H_2[8]. The CO_2 plays the role of providing replenishment of the used oxygen surface species, thus yielding additional CO [9]. A problem for all these systems is coke formation and thus the deactivation of the catalyst due to a decrease in catalytically active surface area. Especially Ni-based catalysts tend to show a lot of coking during the partial oxidation of methane [10]. A strategy to reduce this effect is the addition of alkaline earth metal oxides [11]. With perovskite catalysts, it is possible to combine the high activity of Ni with the coke reduction of alkaline earth metal oxides.

Perovskite oxides are crystalline substances with the general formula ABO_3 with A and B being cations of different size [12]. The A and B-sites can each be prepared with one element each or a mixture of elements in the style of $(A_xA'_{1-x})(B_xB'_{1-x})O_3$. In these types of perovskites it was shown that exsolution of the B-site elements is possible by selective reduction of these elements (e. g. in an atmosphere containing H_2 at elevated temperatures, [13] and migration to the surface, resulting in the formation of metal nanoparticles of the respective elements on the surface [12]. These nanoparticles can greatly enhance the catalytic activity. Alkaline earth metals can be added as A-site cations to achieve the abovementioned combination.

Such perovskite catalysts are relatively cheap and easily prepared. In comparison with a Ni impregnated perovskite (e.g. prepared by conventional incipient wetness impregnation) under the same conditions, Wei et. al. [14] found a more uniform distribution of Ni nanoparticles and a higher resistance to carbon deposition for the Ni doped perovskite $La_{0.9}Mn_{0.8}Ni_{0.2}O_3$ after exsolution. They explain this behaviour with the reason that the Ni nanoparticles formed from exsolution are partially embedded into the perovskite support, which hinders carbon fibre formation, whereas the loosely bound Ni nanoparticles originating from impregnation promoted the formation of carbon nanotubes with Ni particles on top. Furthermore, these well-socketed particles show an increased resistance towards sintering [15]. Another advantage is that regeneration of the catalyst is simple and can be achieved by oxidation-reduction-cycles, where the exsolved metal is incorporated into the perovskite support again upon oxidation and subsequently exsolved as new particles.

In this study, Ni-doped perovskite materials were investigated regarding their catalytic activity for MDR. The catalysts had an A-site composition of 60 % Nd and 40 % Ca and the B-site consisted of Fe doped with different amounts of Ni. This leads to the general formula for the used perovskites of $Nd_{0.6}Ca_{0.4}Fe_{1-x}Ni_xO_{3-\delta}$ with x = 0.1 or x = 0.03. Three different catalysts were prepared. One with 10 % Ni (NCFNi10) on the B-site and two with 3 % Ni (NCFNi3) on the B-site. This allows for the comparison of the effect of different Ni concentrations on the catalyst activity. The two catalysts with 3 % Ni differ in the preparation. Both were calcined during synthesis at 800 °C, but one was used after calcination (NCFNi3-calc) and the other was additionally sintered at 1250 °C (NCFNi3-sint) to study the effect of the sintering on the catalytic behaviour. Besides catalytic tests, the materials were characterized with X-ray diffraction (XRD) and scanning electron microscopy (SEM) before and after the reaction cycles.

2 Methods

2.1 Synthesis

As in previous work [16], the Pechini synthesis [17] was used to prepare the investigated perovskite powders. The following chemicals were used as starting materials to synthesise the materials with the wanted compositions: Nd_2O_3 (99.9 %, Strategic Elements, Deggendorf, Germany), $CaCO_3$ (99.95 %, Sigma-Aldrich, St. Louis, MO, USA), Fe (99.5 %, Sigma-Aldrich, St. Louis, MO, USA) and $Ni(NO_3)_3 \cdot 6H_2O$ (98 %, Alfa Aesar, Haverhill, MA, USA). Solutions of the appropriate amounts of the compounds were prepared in HNO_3 (doubly distilled, 65 %, Merck, Darmstadt, Germany). Subsequent steps included the addition of citric acid (99.9998 % trace metals pure, Fluka, Honeywell International, Charlotte, NC, USA) in excess of 20 % to form cation complexes, removing H_2O by evaporation, and heating of the resulting gel until self-ignition. Then, the formed powders underwent heat treatment (calcination in air at 800 °C for 3 h). Afterwards, the NCFNi10 material was treated a second time at 1000 °C for 3 h and the NCFNi3-sint material was sintered at 1250 °C for 12 h. After the final annealing, each sample was ground with a mortar to achieve homogeneity for better characterization.

2.2 Characterization Methods

Powder XRD measurements and SEM experiments were carried out as described in previous work [16]. The powder XRD measurements were done at room temperature in air on a PANalyticalX'Pert Pro diffractometer (Malvern Panalytical, Malvern, UK) in Bragg–Brentano geometry using a mirror for separating the Cu $K_{\alpha 1,2}$ radiation and an X'Celerator linear detector (Malvern Panalytical, Malvern, UK). Data analysis was conducted with the HighScore Plus software (Malvern Panalytical, Malvern, UK) [18] and the PDF-4+ 2019 database (ICDD—International Centre for Diffraction Data, Newtown Square, PA, USA) [19]. The database entries were used to ascribe the reflexes in the diffractograms. The SEM images were recorded using secondary electrons on a Quanta 250 FEGSEM (FEI Company, Hillsboro, OR, USA) with an acceleration voltage of 5 kV for sufficient surface-sensitivity.

To determine the actual composition of the synthesised samples, ICP-OES was used. The samples were digested in HCl and, after diluting, analysed with an iCAP 6500 ICP-OES spectrometer (Thermo Scientific, Waltham, MA, USA) equipped with a Meinhardt nebulizer and a cyclonic spray chamber (Glass Expansion, Port Melbourne, Australia). Observed signal intensities were converted into concentration units by means of external aqueous calibration.

2.3 Catalytic Testing

Catalytic tests for methane dry reforming (cf. Equation 1) were performed in a 6 mm tubular flow reactor (quartz glass, inner diameter 4 mm) at atmospheric pressure. Online gas analysis was conducted by a Micro-GC (Fusion 3000A, Inficon) which was continuously sampling every 2–3 min. The reactive gas flow was 10.5 ml min^{-1}, with a CH_4 flow of 3 ml min^{-1}, a CO_2 flow of 1.5 ml $min^{-1}$and a carrier gas flow of 6 ml min^{-1}Ar (all gases provided by Messer Group GmbH). For catalytic reactions, the pure perovskite powder catalysts (100–200 mg) were supported directly on a quartz wool bed. The amount of catalyst material for each respective experiment was chosen in a way such that during reaction the thermodynamic limit of the dry methane reforming reaction was not reached, enabling catalytic comparison. A PID controller (EMSR EUROTHERM GmbH) was used to control the reac-

tor heater. To do so, a K-type thermocouple was reaching directly into the catalyst bed. Prior to all catalytic testing, each catalyst was oxidized for 30 minutes in O_2 (p = 1 bar) at 400 °C to ensure the same oxidation state as a starting point for all materials. Afterwards, the catalysts were optionally reduced for 60 minutes in H_2/H_2O (ratio 32:1) at 625 °C.

For the present study, three types of experiments were carried out. The activity of the perovskites was tested with heating up the oxidized and/or reduced catalyst under reactive gas flow from 400 °C to 700 °C with a rate of 1 °C min^{-1}. To test, if the reaction conditions lead to a reduction of the perovskite, experiments were conducted with each catalyst, prepared without the reducing pre-treatment and using the same temperature ramp under reactive gas flow as for the reduced catalyst. Two consecutive runs were performed in this type of experiment, to investigate the effect of a potential reduction of the material. The stability of the reduced perovskites under reaction conditions was tested by switching to reactive gas flow and 600 °C after the reductive pre-treatment and holding the temperature steady for about 3 hours.

To be able to directly compare the different perovskite catalysts, a specific activity (mol s^{-1} m^{-2}) was calculated. In order to do so, the specific surface areas a_S (in m^2 g^{-1}) of the materials (Tab. 1) were measured according to the BET method [20] by fitting measured adsorption isotherms to a BET model. The isotherms were recorded using a Micrometrics ASAP 2020 system. The samples were degassed at 300 °C under vacuum for 4 h, followed by measuring full N_2 adsorption-desorption isotherms at -196 °C (liquid N_2). Together with the known mass of used catalyst material m_{Cat} in g and total corrected product gas flow $\dot{n}$ in mol s^{-1} (correction for the conversion depended change of the reaction volume), the CO formation (mole fraction x_{CO} in the product stream) was normalized to the catalyst surface area a_{Cat} according to Equation 2, giving a specific activity r_{CO} in mol s^{-1} m^{-2}, i.e. how many moles of product (CO) were formed per s and per m² surface.

$$r_{CO} = \frac{\dot{n} \cdot x_{CO}}{a_{Cat}} = \frac{\dot{n} \cdot x_{CO}}{a_S \cdot m_{Cat}} \quad (2)$$

3 Results

3.1 Characterization of the Pristine Catalysts

The pristine catalysts after synthesis have been characterized by ICP-OES (elemental composition, Tab. 1), XRD (crystal phases, Fig. 1), SEM (morphology, Fig. 2) and BET (specific surface area, Tab. 1). All materials contain the intended amount of Ni doping on the B-site, 10 % or 3 %, respectively. The A-site composition of the two NCFNi3 materials almost agree with the nominal composition as well. However, the NCFNi10 material is slightly A-site sub-stoichiometric, with a total A-site cation deficit of 7 %.

Table 1. Characteristics of the pristine samples: Composition according to ICP-OES measurements, specific surface area determined with the BET method and cell parameters of the units cells, found with Rietveld refinement.

Sample	Composition – ICP-OES	BET Area a_S / m^2g^{-1}	Cell Parameters a / Å	b / Å	c / Å
NCFNi10	$Nd_{0.55}Ca_{0.38}Fe_{0.90}Ni_{0.10}O_{3-\delta}$	1.57	5.523	7.726	5.438
NCFNi3-calc	$Nd_{0.60}Ca_{0.39}Fe_{0.97}Ni_{0.03}O_{3-\delta}$	2.44	5.551	7.753	5.453

NCFNi3-sint	$Nd_{0.59}Ca_{0.40}Fe_{0.97}Ni_{0.03}O_{3-\delta}$	0.357	5.477	7.679	5.413

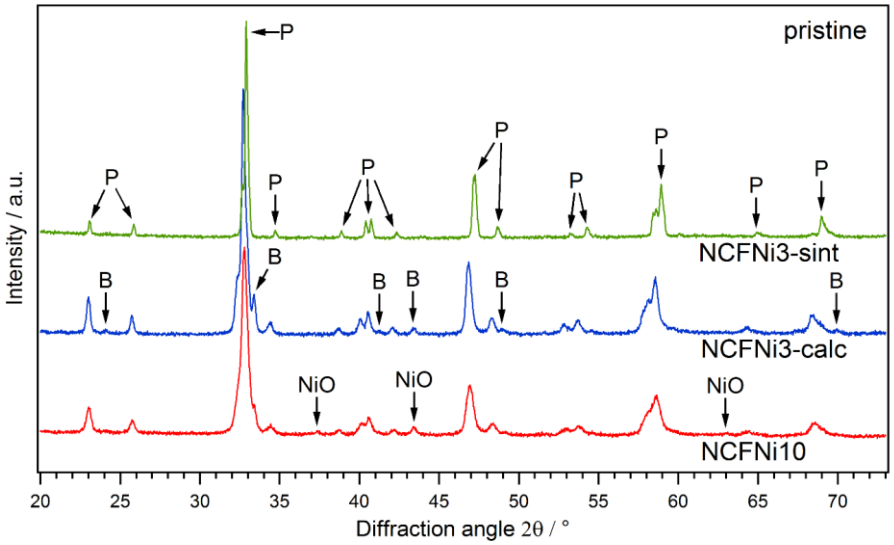

Fig. 1. XRD patterns of the pristine samples. Reflexes marked with "P" belong to the main perovskite phase, reflexes marked with "B" are belong to a brownmillerite phase with ordered oxygen vacancies. The NCFNi10 sample additionally contains a NiO phase.

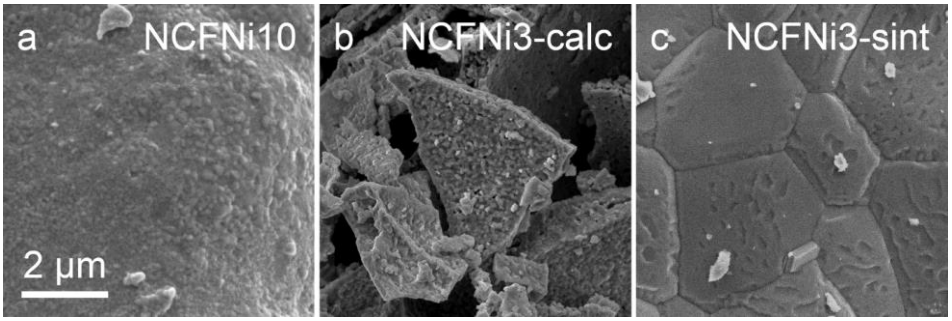

Fig. 2. SEM images of the pristine samples: a) NCFNi10 is dense with globular crystallites, b) NCFNi3-calc has the smallest crystallites and some pores and c) NCFNi3-sint has very large polyhedral crystallites.

The main phase in all materials is a perovskite phase with an orthorhombic lattice (reflexes labelled with "P" in the diffractograms). The largest reflex is at 2θ of 32.8°, 32.7° and 33.0° for NCFNi10, NCFNi3-calc and NCFNi3-sint, respectively. This shift to higher angles in the order NCFNi3-calc, NCFNi10 and NCFNi3-sint is also seen for the other reflexes and reflects the cell parameters found by Rietveld refinement (Tab. 1), which are decreasing in the same order. This trend coincides with the maximum annealing temperature of the different samples (800 °C, 1000 °C and 1250 °C, respectively). Probably a higher annealing temperature leads to fewer defects in the structure and results in the reduced cell volume.

The NCFNi3-sint material is a phase pure perovskite. However, in the diffractogram of NCFNi3-calc weak reflexes of an additional phase were observed. These are labelled with "B" and could be assigned to a brownmillerite type phase. Its structure can be derived from a perovskite structure with ordered oxygen vacancies. This leads to the conclusion that the amount of oxygen vacancies in this material is higher than in NCFNNi3-sint. Here, the

higher annealing temperature of the latter may have played a role as well, enabling a more oxidized state of the perovskite (i.e. less vacancies), and the amount of oxygen vacancies might be connected with the change in the cell parameters.

In the NCFNi10 material, besides the main perovskite phase small amounts of NiO were found (largest reflex at 2θ of 43.4°). Due to the higher amount of doping, not all of the doping element could be incorporated into the perovskite lattice. Additionally, the A-site sub-stoichiometry impeded the full incorporation of the B-site cations. Very weak reflexes of the brownmillerite phase can be seen here as well (e.g. the shoulder at 2θ of 33.4°).

The effect of different annealing temperatures is also visible in the SEM images of the different materials. While NCFNi3-calc (Fig. 2b) has small globular crystallites and some pores, NCFNi10 (Fig. 2a) is dense and the crystallites are slightly larger on average, but still globular. However, in NCFNNi3-sint (Fig. 2c), were extensive sintering occurred, the crystallites are much larger and have polyhedral shapes. The larger crystallites are also the reason, why the reflexes in the diffractogram of NCFNi3-sint have a smaller full width at half maximum (FWHM) than for the other materials. Similarly, the specific surface area decreases with higher annealing temperature, due to the larger crystallites and less porosity.

3.2 Catalytic Results and Characterization after Reaction

The results of the catalytic test for MDR during the temperature ramp experiments can be seen in Figure 3. As expected, the CO formation, characterized by the specific activity, increased with increasing temperature for all runs. The NCFNi3-calc material had the lowest activity. Without reductive pre-treatment, only above 600 °C there was a detectable amount of CO in the product stream and even at 700 °C the specific activity was below $1 \cdot 10^{-7}$ mol s^{-1} m^{-2}. The second run in this experiment gave an almost identical result, indicating that no activating reduction of the perovskite occurred during the first run. However, after a reductive pre-treatment the specific activity was higher during reaction, having a value of $7 \cdot 10^{-7}$ mol s^{-1} m^{-2} at 700 °C.

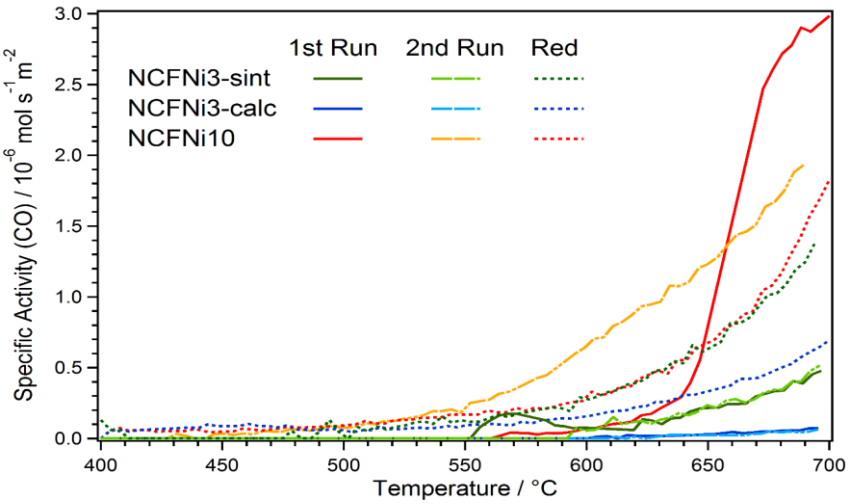

Fig. 3. Results of the catalytic tests for MDR. The specific activity for CO formation is shown for all three tested materials during the temperature ramps from 400 °C to 700 °C. For each material, graphs are shown for the experiment with only oxidative pre-treatment and two consecutive cycles ("1st Run" and "2nd Run"), as well as for the experiment with oxidative and reductive pre-treatment ("Red"). An activation due to the reductive pre-treatment could be observed.

For NCFNi3-sint, the first run with the oxidized material exhibited an activation effect between 550 °C and 600 °C. In this temperature range, the CO formation quickly increased and dropped again. A reason for the observed effect could have been the reduction of the perovskite by CH_4, accompanied by the exceeding formation of CO. This reduction had an activating effect on the catalyst, as the specific activity above 600 °C followed again the expected progression, but at a much larger level than for NCFNi3-calc without reductive pre-treatment, almost reaching the values of the reduced NCFNi3-calc with $5 \cdot 10^{-7}$ mol s^{-1} m^{-2} at 700 °C. Similar as with NCFNi3-calc, the second run gave an almost identical result as the first, but without the activation phenomenon. The CO formation started only at 590 °C and then matched the values of the first run. Again, it could be demonstrated that the activating effect of a reductive pre-treatment was larger than the effect of the reduction in reaction atmosphere. Thus, the specific activity could be increased even more, reaching a value of $1.4 \cdot 10^{-6}$ mol s^{-1} m^{-2} at 700 °C, which was twice as high as for NCFNi3-calc.

In case of NCFNi10, CO formation started at 560 °C. Possibly, this was also due to an activating reduction, although the according CO formation bump was very small. The curve then shortly followed the progression of the NCFNi3-sint curve, but starting from 620 °C a huge activation phenomenon could be observed, with a massive increase of CO formation up to a specific activity of $3.0 \cdot 10^{-6}$ mol s^{-1} m^{-2} at 700 °C. The maximum increase in CO formation was around 660 °C. Consequently, in the second run some CO formation was found already around 450 °C and the specific activity was much larger than for the other runs at all temperatures (with the exception of the activation phenomenon of the first run). At 700 °C the specific activity was at $2.1 \cdot 10^{-6}$ mol s^{-1} m^{-2}. When applying the reductive pre-treatment on NCFNi10, the resulting curve almost perfectly matched the results of the experiment with NCFNi3-sint after reduction. Only at the highest temperatures the NCFNi10 catalyst was better, starting to deviate around 670 °C and reaching $1.8 \cdot 10^{-6}$ mol s^{-1} m^{-2} at 700 °C. Interestingly, here the activation in the reaction atmosphere lead to a higher catalytic activity than in the experiments including reductive pre-treatment.

For all catalysts, when doing the ramp experiment with the pre-reduced material, there is some higher than expected CO formation at lower temperatures (i.e. below 500 °C). This can be attributed to the formation of oxygen vacancies in the perovskite lattice upon reduction and the subsequent reoxidation with CO_2 during reaction, leading to increased values of CO. The formation of oxygen vacancies during reductive pre-treatment is one of the reasons for the enhanced catalyst performance after reduction, because they support the activation of CO_2 for reaction [21]. This effect similarly occurs in all materials. Besides oxygen vacancies, another activating effect for the catalysts is the exsolution of metal nanoparticles. In particular, these enhance the degradation of CH_4. Formation of nanoparticles more strongly affects the catalytic activity than oxygen vacancies and the different exsolution behaviour is the main reason for the differences in catalytic performance between the various samples. To investigate the effect of exsolution, the perovskites were characterized again with SEM (Fig. 4) and XRD (Fig. 5) after the catalytic tests.

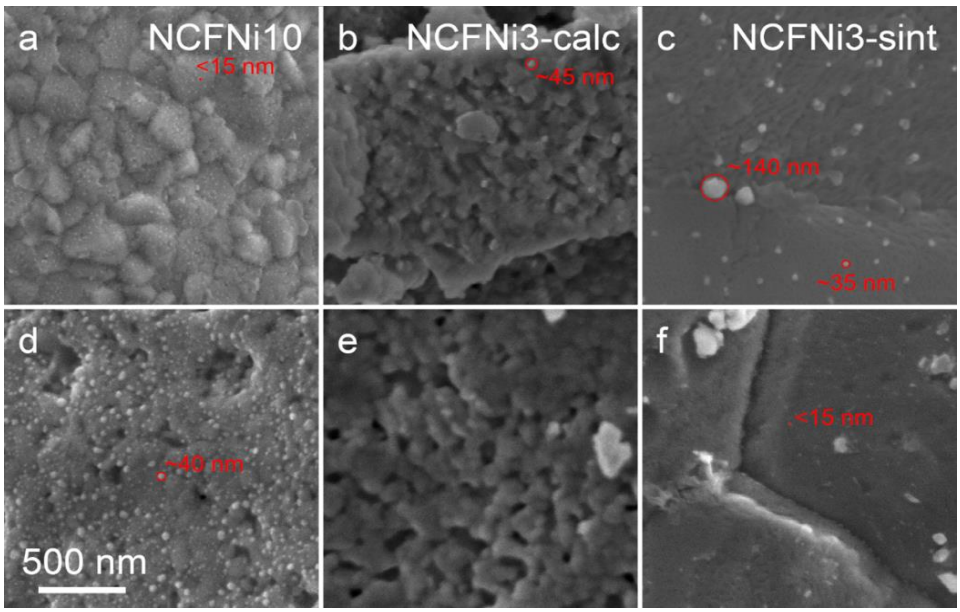

Fig. 4. SEM Images of the catalyst after MDR. The first row displays images of a) NCFNi10, b) NCFNi3-calc and c) NCFNi3-sint after the ramp experiments with the pre-reduced materials. The second row highlights images of d) NCFNi10, e) NCFNi3-calc and f) NCFNi3-sint using the catalyst without reductive pre-treatment (i.e. after two consecutive runs without pre-reduction).

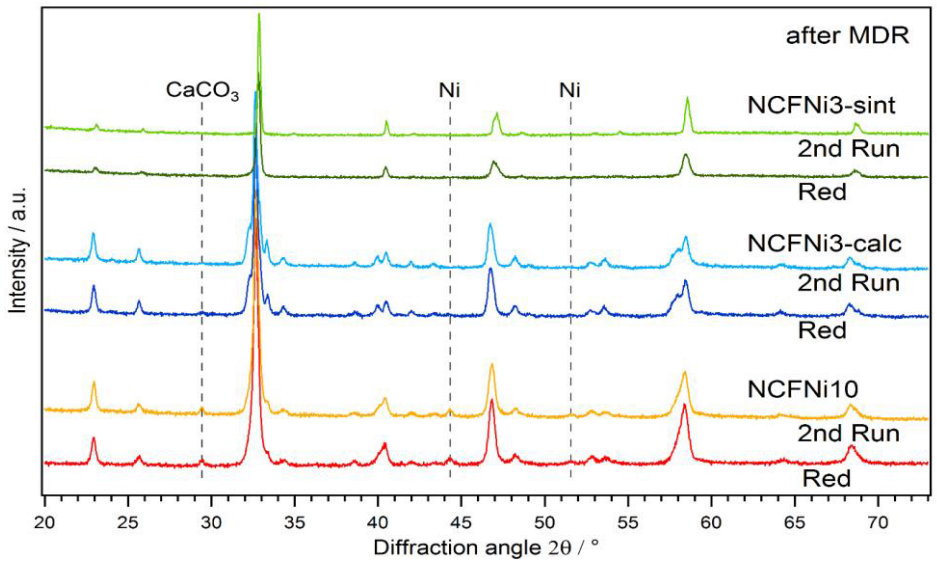

Fig. 5. Diffractograms of the various catalysts after the MDR experiments, either after the temperature ramp with the reduced materials or after the second run using the oxidized samples. Observed new phases were metallic Ni and $CaCO_3$ for NCFNi10 and NCFNi3-calc, while NiO disappeared for NCFNi10. NCFNi3-sint underwent a phase transition from an orthorhombic to a rhombohedral structure.

For NCFNi10, nanoparticles are visible in the SEM images, both after the experiment with the reduced catalyst (Fig. 4a) and after the second run in the experiment without reductive pre-treatment (Fig. 4d). While in the first case, the particles are very small (diame-

ters below 15 nm, an accurate determination is not possible due to the limited resolution of the microscope), in the latter case the particles are bigger (diameters around 40 nm). In both images, they exhibit a dense and homogeneous distribution. In the corresponding XRD patterns, a metallic Ni phase is visible as small signals at 2θ of 44.3° and 51.6°. At the same time, the reflexes of the main perovskite phase did not change compared to the state before reaction. Furthermore, the NiO phase observed in the pristine catalyst is not present anymore. These results suggest that the direct reduction of NiO to Ni combined with Ni exsolution from the perovskite phase lead to the formation of Ni nanoparticles decorating the surface, being responsible for the tremendous increase in activity for MDR. This process was supported by the A-site sub-stoichiometry and also the perovskite backbone remained stable. The huge activation phenomenon seen in the catalytic test without reductive pre-treatment can be attributed to the formation of the larger particles in Figure 4d. These larger particles resulted then in a higher specific activity during the catalytic test.

The SEM images of the NCFNi3-calc catalyst reveal only fewer particles after the catalytic test run with reductive pre-treatment (Fig. 4b) and none at all after the runs without pre-reduction (Fig. 4e). This agrees with the results from XRD experiments, were traces of a metallic Ni phase is only visible in the first case. However, here the Ni particles solely originate from exsolution. These observations explain the results of the catalytic tests. For NCFNi3-calc, the reaction atmosphere was not sufficiently reducing to trigger exsolution, hence no activation phenomena and no exsolved particles were observed and the catalytic activity was very low. The few particles after reduction increased the activity, but not as much as for NCFNi10 with a much denser particle distribution.

Nanoparticles can also be seen in the SEM images of NCFNi3-sint in both cases (Figs 4c, 4f). Here, the particles exsolved in reducing reaction atmosphere are smaller (diameters below 15 nm) compared to those formed during the reductive pre-treatment (around 35 nm). For this material, with very clear grain boundaries, the influence of these grain boundaries can be observed. In Figure 4c, two large particles are visible on the grain boundary, the larger one having a diameter of 140 nm. In Figure 4f, a dense streak of the small particles appears alongside the grain boundary. It is reasonable to assume that the grain boundary acts as a primary nucleation side for the nanoparticle formation, explaining this behaviour. Again, the activation phenomenon in the catalytic measurements can be attributed to the particle formation and the particles cause an increase in catalytic activity – the larger particles after reductive pre-treatment resulted in a higher specific activity.

Interestingly, no Ni phase was found in the XRD patterns of NCFNi3-sint after MDR. Possibly, the signal was too weak to be distinguishable from the noise. However, the perovskite underwent a phase transition towards a rhombohedral structure, induced by the reducing atmosphere. The transition is complete for the pre-reduced catalyst, while in the case of no reductive pre-treatment some small reflexes of the orthorhombic structure remain. This different behaviour (compared to the materials that were annealed at lower temperatures) is probably related to the more perfect crystal structure after the high annealing temperature. Further experiments are necessary to fully understand this phase transition behaviour and its influence on exsolution and catalytic performance.

Correlating the distribution of the exsolved particles and the specific activity during MDR leads to the conclusion that the activity increases both with increased particle size and particle density. The pre-reduced NCFNi10 and NCFNi3-sint have almost the same activity, but the first showed smaller and denser particles, while the latter has fewer although bigger ones. In neither of the SEM images signs of sintering or coking can be seen, even for the very dense distributions, proving the superior stability of the exsolved particles during reaction conditions. However, in the XRD patterns of NCFNi10 and NCFNi3-calc, a $CaCO_3$ phase appeared after the reaction. This known segregation of the alkaline earth metal

in A-site doped perovskites [22] is accelerated by the attempt to re-establish stoichiometry after exsolution of the B-site metal.

For catalytic applications a crucial property is the long term reaction stability of catalyst materials [23]. Therefore, we tested one of the novel materials during MDR at 600 °C for a longer time period (Fig. 6). There occurs a deactivation over time, observable as a decrease of the specific activity for CO formation. The main reason for this deactivation is the formation of $CaCO_3$ on the catalyst surface, as indicated by XRD and by SEM (inset, Fig. 6b). In the SEM image, larger smooth crystallites of $CaCO_3$ are visible. There are none of the small particles on their surface, thus they reduce the catalytically effective surface area and cause therefore a deactivation of the catalyst.

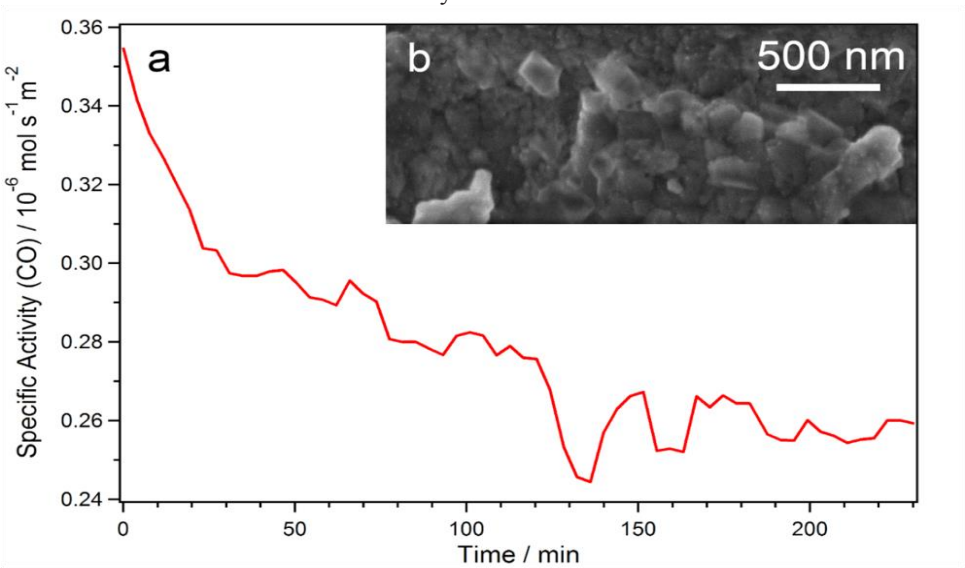

Fig. 6. Results of the stability test with NCFNi10 in MDR reaction environment. a) Specific activity for CO formation over time. b) SEM image of the catalyst after the experiment.

4 Conclusions

Three Fe based perovskites, NCFNi10, NCFNi3-calc and NCFNi3-sint, with a varying amount of Ni doping and different sintering temperatures were successfully synthesized and tested for their catalytic performance for MDR. The materials can be activated via a reductive treatment. Several mechanisms contribute to the increased catalytic activity after reduction: First, the formation of oxygen vacancies, increasing the CO_2 activation capability of the surface. Second, the formation of Ni nanoparticles, either by a reduction of a present NiO phase or by exsolution. Similarly, de Lima et al. [24]reported these different reduction mechanisms during temperature programmed reduction experiments on perovskites.

The formed nanoparticles accelerate the catalytic degrading CH_4 on the surface and are thus crucial for a high catalytic activity. The increase in activity is larger with bigger Ni particles and a denser distribution on the surface. These properties of the formed nanoparticles can be influenced on one hand by the choice of material and on the other by choice of the reduction environment.

Ni particle formation is facilitated by a higher amount of Ni doping and by using an A-site sub-stoichiometric perovskite, as it was the case for NCFNi10. Another factor is the annealing temperature during material preparation. As observed with NCFNi3-calc and NCFNi3-sint, a higher annealing temperature resulted in larger crystallites with less defects,

while at the same time exsolution was easier. Furthermore, the perovskite annealed at the higher temperature showed a different reduction behaviour, exhibiting a phase transition from an orthorhombic to a rhombohedral structure. It can be assumed that the changed structure is connected with the improved exsolution property, but further experiments are necessary to support this.

In all cases, the formed nanoparticles exhibited a high resistance towards coking and sintering. This makes these exsolution catalysts very promising candidates for further applications. However, the particle formation was accompanied by the segregation of $CaCO_3$, which is blocking the catalyst surface and resulting in a deactivation of the catalyst over time.

References

1. D. Pakhare, J. Spivey A review of dry (CO2) reforming of methane over noble metal catalysts. *Chemical Society Reviews,* **43(22)**, 7813-7837 (2014)
2. C. Rameshan, H. Li, K. Anic, M. Roiaz, V. Pramhaas, R. Rameshan, R. Blume, M. Haevecker, J. Knudsen, A. Knop-Gericke, G. Rupprechter. In situ NAP-XPS spectroscopy during methane dry reforming on ZrO2/Pt(111) inverse model catalyst. *Journal of Physics-Condensed Matter,* **30(26)**, (2018)
3. F. Solymosi, G. Kutsan, A. Erdohelyi CATALYTIC REACTION OF CH4 WITH CO-2 OVER ALUMINA-SUPPORTED PT METALS. *Catalysis Letters,* **11(2)**, 149-156 (1991)
4. A. Kuzhaeva, N. Dzhevaga, I. Berlinskii The processes of hydrocarbon conversion using catalytic systems. *International Scientific Conference on Applied Physics, Information Technologies and Engineering (Apitech-2019),* **1399**, (2019)
5. J.W. Nam, H. Chae, S.H. Lee, H. Jung, K.Y. Lee Methane dry reforming over well-dispersed Ni catalyst prepared from perovskite-type mixed oxides. *Natural Gas Conversion V,* **119**, 843-848 (1998)
6. A.C. Luntz, J. Harris CH4 DISSOCIATION ON METALS - A QUANTUM DYNAMICS MODEL. *Surface Science,* **258(1-3)**, 397-426 (1991)
7. D.C. Seets, M.C. Wheeler, C.B. Mullins Mechanism of the dissociative chemisorption of methane over Ir(110): Trapping-mediated or direct? *Chemical Physics Letters,* **266(5-6)**, 431-436 (1997)
8. M.C.J. Bradford, M.A. Vannice CO2 reforming of CH4. *Catalysis Reviews-Science and Engineering,* **41(1)**, 1-42 (1999)
9. A. Horvath, G. Stefler, O. Geszti, A. Kienneman, A. Pietraszek, L. Guczi Methane dry reforming with CO2 on CeZr-oxide supported Ni, NiRh and NiCo catalysts prepared by sol-gel technique: Relationship between activity and coke formation. *Catalysis Today,* **169(1)**, 102-111 (2011)
10. J.B. Claridge, M.L.H. Green, S.C. Tsang, A.P.E. York, A.T. Ashcroft, P.D. Battle A STUDY OF CARBON DEPOSITION ON CATALYSTS DURING THE PARTIAL OXIDATION OF METHANE TO SYNTHESIS GAS. *Catalysis Letters,* **22(4)**, 299-305 (1993)
11. E. Ruckenstein, Y.H. Hu Carbon dioxide reforming of methane over nickel alkaline earth metal oxide catalysts. *Applied Catalysis a-General,* **133(1)**, 149-161 (1995)
12. L.G. Tejuca, J.L.G. Fierro, J.M.D. Tascon STRUCTURE AND REACTIVITY OF PEROVSKITE-TYPE OXIDES. *Advances in Catalysis,* **36**, 237-328 (1989)

13. B. Hua, M. Li, Y.F. Sun, J.H. Li, J.L. Luo Enhancing Perovskite Electrocatalysis of Solid Oxide Cells Through Controlled Exsolution of Nanoparticles. *Chemsuschem*, **10(17)**, 3333-3341 (2017)
14. T. Wei, L.C. Jia, H.Y. Zheng, B. Chi, J. Pu, J. Li, LaMnO3-based perovskite with in-situ exsolved Ni nanoparticles: a highly active, performance stable and coking resistant catalyst for CO2 dry reforming of CH4. *Applied Catalysis a-General*, **564**, 199-207 (2018)
15. D. Zubenko, S. Singh, B.A. Rosen Exsolution of Re-alloy catalysts with enhanced stability for methane dry reforming. *Applied Catalysis B-Environmental*, **209**, 711-719 (2017)
16. L. Lindenthal, R. Rameshan, H. Summerer, T. Ruh, J. Popovic, A. Nenning, S. Loffler, A.K. Opitz, P. Blaha, C. Rameshan Modifying the Surface Structure of Perovskite-Based Catalysts by Nanoparticle Exsolution. *Catalysts*, **10(3)**, (2020)
17. M.P. Pechini *Method of preparing lead and alkaline earth titanates and niobates and coating method using the same to form a capacitor*. (U.S. Patent No. 3.330.697(304434), 1967)
18. T. Degen, M. Sadki, E. Bron, U. König, G. Nénert The HighScore suite. *Powder Diffraction*, **29**, S13-S18 (2014)
19. *PDF-4+ 2019*. (ICDD, 2018)
20. S. Brunauer, P.H. Emmett, E. Teller Adsorption of gases in multimolecular layers. *Journal of the American Chemical Society*, **60**, 309-319 (1938)
21. L.J. Liu, C.Y. Zhao, Y. Li Spontaneous Dissociation of CO2 to CO on Defective Surface of Cu(I)/TiO2-x Nanoparticles at Room Temperature. *Journal of Physical Chemistry C*, **116(14)**, 7904-7912 (2012)
22. J. Popovic, L. Lindenthal, R. Rameshan, T. Ruh, A. Nenning, S. Loffler, A.K. Opitz, C. Rameshan High Temperature Water Gas Shift Reactivity of Novel Perovskite Catalysts. *Catalysts*, **10(5)**, (2020)
23. H. Lorenz, Q.A. Zhao, S. Turner, O.I. Lebedev, G. Van Tendeloo, B. Klotzer, C. Rameshan, K. Pfaller, J. Konzett, S. Penner Origin of different deactivation of Pd/SnO2 and Pd/GeO2 catalysts in methanol dehydrogenation and reforming: A comparative study. *Applied Catalysis a-General*, **381(1-2)**, 242-252 (2010)
24. S.M. de Lima, J.M. Assaf Ni-Fe catalysts based on perovskite-type oxides for dry reforming of methane to syngas. *Catalysis Letters*, **108(1-2)**, 63-70 (2006)